



Synthesis of Ce_aMnO_x hollow microsphere with hierarchical structure and its excellent catalytic performance for toluene combustion



Lele Zhao, Zhiping Zhang, Yushi Li, Xuesong Leng, Tianrui Zhang, Fulong Yuan, Xiaoyu Niu*, Yujun Zhu*

Key Laboratory of Functional Inorganic Material Chemistry (Heilongjiang University), Ministry of Education, School of Chemistry and Materials, Heilongjiang University, Harbin, 150080, PR China

ARTICLE INFO

Keywords:

Ce_aMnO_x hollow microsphere
Hierarchical structure
Strong interaction
Catalytic combustion
Toluene

ABSTRACT

A series of Ce_aMnO_x hollow microsphere like arbutus with hierarchical structure are prepared by redox co-precipitation method and applied for catalytic toluene combustion. The $\text{Ce}_{0.03}\text{MnO}_x$ shows a better catalytic performance for toluene combustion with high stability, water resistance, even under the condition of 5 vol.% H_2O . The results of XRF, XRD, Raman, N_2 adsorption-desorption, SEM, TEM prove that the doping of Ce can affect the structure of Ce_aMnO_x such as much smaller particle size and higher specific surface area. The characterizations of $\text{H}_2\text{-TPR}$, $\text{O}_2\text{-TPD}$, XPS certify the strong interaction between Ce and Mn oxides that leads to more surface adsorbed oxygen and Mn^{4+} species due to oxidation reduction cycle of $\text{Mn}^{3+} + \text{Ce}^{4+} \leftrightarrow \text{Mn}^{4+} + \text{Ce}^{3+}$ after Ce addition. Meanwhile, the Toluene-TPD in different conditions confirms the introduction of water promoted the catalytic oxidation of toluene. *In situ* DRIFTS is used to investigate the reaction process of toluene oxidation. And the results reveal that the $\text{Ce}_{0.03}\text{MnO}_x$ catalyst has much stronger ability to adsorb and activate toluene compared with MnO_x catalyst, especially under with H_2O . That may be the main reason that the $\text{Ce}_{0.03}\text{MnO}_x$ catalyst exhibits the special catalytic activity for toluene combustion.

1. Introduction

Volatile organic compounds (VOCs) are a group of chemicals such as hydrocarbon, esters, aldehydes, etc., which are released from industrial process, incomplete combustion, paint materials and other activities related to human [1,2]. VOCs are regarded as not only one of the most contributors to air pollution, but also the main hazardous substances with great damage effect on public health [2,3]. Accordingly, it is impending to reduce effectively VOCs emission. Nowadays, several abatement technologies such as photocatalysis [4–6], thermal oxidation, wet scrubbing [7], catalytic oxidation and so on have been used to control the release of VOCs.

Among all the applied control technologies, catalytic oxidation is considered one of the most hopeful environmental technologies for VOC treatment because of its higher treatment efficiency, lower reaction temperature and less energy consumption [8]. In the past few years, a large number of catalysts about VOCs catalytic oxidation have been reported by the researchers. Generally, catalysts for VOCs combustion are classified into two categories including noble metals (Pt, Au, Pd, Ag) [9–14] and transition metal oxide catalysts. However, the

usage of the noble metal as catalyst is limited due to high cost, low thermal stability and easy deactivation. Compared with noble metals, transition metal oxide catalysts have attracted extensive attention because of its high catalytic activity, lower costs and higher resistance to poisons.

In these transition metal oxide catalysts, Mn [15–19], Ce [20–22], Cu [23,24], Nb [25] and Co [26–31]-base oxides are considered as the most efficient catalysts for VOCs combustion based on their strong oxidation properties. Manganese oxides (MnO_x) are considered as the much better catalysts for catalytic hydrocarbons oxidation at low temperature because of their strong oxidizability derived from the structural property of Mn [32,33]. So in the past ten years, MnO_x with different morphology and structures has been extensively studied in catalytic combustion of hydrocarbons. For example, Dai et al. [15] synthesized a series of manganese oxides including rod-like, wire-like, tubular $\alpha\text{-MnO}_2$, and flower-like spherical Mn_2O_3 by the hydrothermal method and the CCl_4 solution method, which were used remove toluene and the rod-like $\alpha\text{-MnO}_2$ showed the better catalytic performance due to its high adsorbed oxygen concentration. Li's group [16] prepared 3DOM $\gamma\text{-MnO}_2$ -like *via* hard template, which was also responsible for

* Corresponding authors.

E-mail addresses: niuxiaoyu@hlju.edu.cn (X. Niu), yujunzhu@hlju.edu.cn (Y. Zhu).

the excellent catalytic performance because of the mesoporous structure and O_{latt} mobility. Tang et al. [17] synthesized high surface area mesoporous manganese oxide by a novel template-free oxalate route, and the catalyst exhibited high stability. In addition, lots of metal oxides materials with hierarchical structure were prepared and used to electrochemistry that displayed specific electrochemical performance compared with traditional oxides [34,35]. In general, manganese oxide with special structure exhibits the much better performance than the traditional MnO_x .

Furthermore, CeO_2 , as a rare earth oxide, has been extensively investigated in heterogeneous catalysis based on its excellent storage/release capacity of oxygen. Wang et al. [36] synthesized Ce_xMn_{1-x} composite oxides via hydrothermal process which exhibited good activity because of crystal defects and synergistic effect between Mn and Ce. Wang et al. prepared Ce-Mn oxides by sol-gel method and exhibited high ability and activity to remove chlorobenzene [37]. Moreover, Chen et al. reported that CeMn composite oxides were synthesized by using hydrolysis driving redox co-precipitation method which showed the excellent performance of catalytic oxidation of VOCs (toluene, benzene, o-xylene and chlorobenzene) [38].

Therefore, we would consider whether the synergistic effect between Ce and Mn oxides could be effective for enhancing the catalytic oxidation ability. In order to improve the synergistic effect, MnO_x modified by Ce with hierarchical structure is considered for design and synthesis based on above description.

In this work, a series of Ce_aMnO_x materials with hierarchical structure are prepared by redox co-precipitation method and applied for catalytic toluene combustion. The relation between catalyst structure and catalytic activity are investigated by various characterizations. The purpose of this paper is to understand the effects of Ce on the structure and the catalytic performance of Ce_aMnO_x .

2. Experimental

2.1. Catalysts preparation

Ce_aMnO_x hollow microspheres like arbutus with hierarchical structure were prepared by redox co-precipitation method. Briefly, 2.500 g $KMnO_4$ and 1.060 g $MnSO_4$ were dissolved by distilled water, and added an appropriate amount of $Ce(NO_3)_3 \cdot 6H_2O$ (0.191–0.478 g) according to the molar ratio of Ce to Mn (0.02, 0.03, 0.04 and 0.05). Concentrated hydrochloric acid was added to the mixture to change the pH. Next, 2 mL polyethylene glycol 400 (PEG 400) was added into the solution and then stirring for two hours. After that, the mixture was filtrated and the solid sample was dried in the oven at 100 °C overnight. Finally, the product was calcined in muffle furnace at 500 °C for 3 h at a ramp of 5 °C min⁻¹ to obtain the Ce_aMnO_x ($a = 0.02, 0.03, 0.04$ and 0.05) catalysts. Additionally, the sample MnO_x was also prepared according to above process without adding $Ce(NO_3)_3 \cdot 6H_2O$.

2.2. Catalyst characterization

X-ray diffraction (XRD) pattern was obtained by a Bruker D8 Advance equipped with a Cu $K\alpha$ ($\lambda = 1.5418 \text{ \AA}$). Raman spectrum was measured using a Jobin Yvon HR 800 micro-Raman spectrometer at 458 nm. The Brunauer-Emmett-Teller (BET) surface area (S_{BET}) was conducted on the Micromeritics Tristar II 3020 instrument at liquid N_2 temperature (-196°C). X-ray fluorescence (XRF) spectrometer was used to detect the chemical composition by Bruker S4 Explorer instrument. Surface atomic concentration and chemical states of the elements were measured by X-ray photoelectron spectrometer by a Kratos-AXIS ULTRA DLD with an Al $K\alpha$ radiation source. Scanning electron microscope (SEM) images were obtained using a Hitachi S-4800 microscope at 20 kV and Transition electron microscope (TEM) images were attained by JEOL JEM-2010 F at an accelerating voltage of 200 kV.

Temperature programmed reduction with H_2 (H_2 -TPR) was performed by the TP-5080 AutoChem adsorption analyzer (Xianquan) equipped with a thermal conductivity detector. Firstly, the catalyst (0.0200 g) was pretreated at the steam of O_2 with the flow rate of 30 mL·min⁻¹ for 30 min at 300 °C and cooled down to 30 °C at the same airstream condition. Then the treated catalyst was heated from 30 °C to 800 °C with a rate of 10 °C min⁻¹ in a 5% H_2/N_2 flow (30 mL·min⁻¹). Temperature programmed desorption of O_2 (O_2 -TPD) was conducted on the TP-5080 AutoChem adsorption analyzer. 0.100 g sample was pretreated under O_2 atmosphere (30 mL·min⁻¹) at 300 °C for 30 min and cooled down to 30 °C at the same airstream condition. Then the treated catalyst was heated from 30 °C to 800 °C with a rate of 10 °C·min⁻¹ in a He flow (30 mL·min⁻¹). Oxygen temperature programmed surface reaction (O_2 -TPSR) test was carried on the same instrument with H_2 -TPR. At first, the catalyst (0.050 g) was pre-treated in He at 300 °C for 30 min and cooled it to 50 °C. Then the sample adsorbed toluene for 15 min and was purged by He for 20 min. Finally, the TPSR run was tested under a flow of 30 mL·min⁻¹ 3 vol% O_2/He ramping at 10 °C min⁻¹ to 500 °C and the signal was detected by a mass spectrometer (MS) at mass-to-charge (m/z) ratios of 18 (H_2O), 28 (CO), 44 (CO₂), 92 (toluene) and 106 (benzaldehyde). Toluene-TPD was detected by the same apparatus with different adsorption conditions (Toluene, Toluene + O_2 , Toluene + $O_2 + H_2O$). After adsorption, He was purged for 20 min. Then the temperature was raised to 500 °C under He and MS signals were detected.

The *in situ* DRIFTS study was carried out through FTIR spectrometer (Nicolet 6700) equipped with a DRIFTS cell (Harrick) and a highly sensitive MCT detector cooled by liquid N_2 in the range of 650–4000 cm⁻¹ with 64 scans. Firstly, the sample was loaded on the IR cell and heated to 300 °C for 30 min in the N_2 atmosphere in order to remove the adsorbed gas, and then the temperature decreased to 220 °C to collect the background. Then, the toluene with N_2 as carrier was introduced to the cell under a flow rate of 100 mL·min⁻¹ at 220 °C for 100 min, and the DRIFTS were recorded. After then, N_2 was inlet about 1 h to remove physical adsorbed toluene. Finally, 20% O_2/N_2 was inlet to the cell to record the spectrum.

2.3. Activity tests of catalytic

The catalytic activities were performed in a tubular fixed bed reactor system connected an online gas chromatography (GC) equipped with a flame ionization detector (FID) and a KB-1 column (30 m × 0.25 mm × 0.25 μm). The gas mixture contained 1000 ppm toluene, 5 vol.% of water vapor (when used), 18 vol.% O_2 and N_2 as balance gas. The total reactive gas was intermixed in tubular fixed bed and the flow velocity was 100 mL·min⁻¹, giving weight hourly space velocity (WHSV) of 20,000 mL·h⁻¹ g⁻¹ with 0.300 g catalyst of 40–60 meshes. The activities were also measured under different WHSV of 40,000 and 80,000 mL·g⁻¹ h⁻¹. Water resistance performance was tested under 5 vol.%, 10 vol.% and 20 vol.% H_2O passing the feed stream through a water saturator at 240 °C.

The toluene conversion ($X_{toluene}$) was calculated at different temperature as below Eq. (1).

$$X_{toluene} = (c(toluene)_{outlet} / c(toluene)_{inlet}) \times 100\% \quad (1)$$

Where, $c(toluene)_{outlet}$ and $c(toluene)_{inlet}$ represent the outlet and inlet concentration of toluene, respectively.

TON values were calculated at 200 and 220 °C as below Eq. (2).

$$TON = \frac{\left(\frac{Pv}{RT}\right)\alpha}{m_{cat}\beta_{Mn}/M_{Mn}} t \quad (2)$$

Where P is saturated vapor pressure of toluene at 5 °C (1.227×10^3 Pa); v is toluene flow rate (8.15 mL·min⁻¹); R is proportional constant (8.314 J mol⁻¹ K⁻¹); α is toluene conversion at different test temperature (200 and 220 °C); T is the temperature (278 K); m_{cat} is catalyst

Table 1Pore structure parameter and XRF results of the Ce_aMnO_x samples.

Sample	Crystal size (nm) ^a	Element contents (at.%) ^b			BET surface area ($\text{m}^2 \text{g}^{-1}$)	BJH pore size (nm)	Pore volume ($\text{m}^3 \text{g}^{-1}$)
		Mn	Ce	Ce/Mn ^c			
MnO_x	21.4	100	–	–	27.8	25.8	0.18
$\text{Ce}_{0.02}\text{MnO}_x$	17.9	98.66	1.34	0.014	47.5	21.7	0.26
$\text{Ce}_{0.03}\text{MnO}_x$	16.6	98.24	1.86	0.019	51.2	18.5	0.24
$\text{Ce}_{0.04}\text{MnO}_x$	13.9	97.17	2.83	0.029	71.3	16.7	0.3
$\text{Ce}_{0.05}\text{MnO}_x$	13.5	97.07	2.93	0.030	79.5	13.9	0.28

^a Calculated by the XRD data.^b Data of element content is determined by the XRF analysis.^c Atomic ratio of Ce to Mn in bulk Ce_aMnO_x .

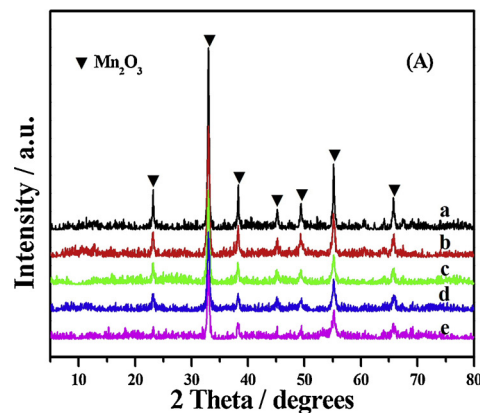
mass; β_{Mn} is the Mn loading content of XPS data; M_{Mn} is relative atomic mass (54.938 g mol⁻¹); t is reaction time which is 1 min.

3. Results and discussion

The element composition of samples in bulk is confirmed by XRF analysis and shown in Table 1. It is easy to see that the molar ratio of Ce to Mn (Ce/Mn) in Ce_aMnO_x is 0.014, 0.019, 0.029 and 0.030 for $\text{Ce}_{0.02}\text{MnO}_x$, $\text{Ce}_{0.03}\text{MnO}_x$, $\text{Ce}_{0.04}\text{MnO}_x$ and $\text{Ce}_{0.05}\text{MnO}_x$, respectively, and it increases gradually with doping more amount of Ce. However, it is noteworthy that the measured Ce/Mn ratio is lower than the corresponding theoretical value (0.02, 0.03, 0.04 and 0.05) in Ce_aMnO_x . Moreover, the Ce/Mn ratio only increases slightly when the theoretical Ce/Mn ratio increases from 0.04 to 0.05 in the synthesis process. In addition, the theoretical Ce/Mn value in the Ce_aMnO_x is used in this paper in order to describe conveniently.

3.1. XRD and Raman results

The crystal phase of these Ce_aMnO_x samples was tested by XRD, and the results are shown in the Fig. 1(A). For all samples, the diffraction peaks at 23.1, 33.0, 38.2 and 55.2° correspond to (211), (222), (400) and (440) planes of bixbyite Mn_2O_3 (PDF 41–1442) [39,40], respectively. As shown in Fig. 1(A), no new characteristic peaks assigned the cerium oxide appeared for Ce_aMnO_x , which may be due to too little Ce content that is beyond the detection limit, Ce element is introduced the lattice of MnO_x , or the Ce oxide highly dispersed in MnO_x . However, the radius of Ce^{3+} (0.134 nm) and Ce^{4+} (0.114 nm) are much larger than that of Mn^{3+} (0.064 nm) and Mn^{4+} (0.060 nm), so Ce can not incorporate into the MnO_x lattice. Moreover, the peak intensity gets weaker and weaker with the increase in the Ce content. The results indicate the existence of Ce could lower the crystallinity of Ce_aMnO_x [41]. The crystal size was calculated by using Scherrer equation with



the peak width at half height of diffraction peaks at 23.1, 33.0 and 38.2°. As displayed in the Table 1, the crystal size is 21.4, 17.9, 16.6, 13.9 and 13.5 nm for MnO_x , $\text{Ce}_{0.02}\text{MnO}_x$, $\text{Ce}_{0.03}\text{MnO}_x$, $\text{Ce}_{0.04}\text{MnO}_x$ and $\text{Ce}_{0.05}\text{MnO}_x$, respectively, suggesting that it decreases gradually with the increase of the Ce content. Interesting, it is found that there is a good linear relation between crystal size and the measured Ce content in Ce_aMnO_x (Fig. 1(B)). To sum up, there is a strong interaction between Ce and Mn oxides and Ce oxide is highly dispersed on the surface of Ce_aMnO_x .

To gain more insight on the structure of catalyst, the samples are characterized by Raman spectroscopy. As presented in Fig. S1, the bands at 365 and 652 cm⁻¹ for MnO_x belong to the out-of-plane bending modes and symmetric stretching of Mn_2O_3 groups, respectively [39,42]. It must be also mentioned that the peaks at 365 and 652 cm⁻¹ for Ce_aMnO_x become weaker than those of MnO_x , suggesting that the strong interaction between Mn and Ce, which is consistent with the results of XRD.

3.2. N_2 adsorption-desorption measurements

Fig. 2 displays the N_2 adsorption-desorption isotherms (Fig. 2(A)) and the pore size distribution (Fig. 2(B)) of the Ce_aMnO_x samples. All samples show the type IV isotherms and possess a distinct H3 type hysteresis loop at relative pressure range at 0.87–1.0, 0.80–1.0, 0.76–1.0, 0.69–1.0 and 0.65–1.0 for MnO_x , $\text{Ce}_{0.02}\text{MnO}_x$, $\text{Ce}_{0.03}\text{MnO}_x$, $\text{Ce}_{0.04}\text{MnO}_x$ and $\text{Ce}_{0.05}\text{MnO}_x$, respectively, indicating that they have similar mesoporous structure [43,44]. Furthermore, the wider range of pore structure is acquired with the leading of Ce, suggesting the pore structure is not neat. Additionally, their average pore sizes are 25.8, 21.7, 18.5, 16.7 and 13.9 nm, and the corresponding specific BET surface area is 27.8, 47.5, 51.2, 71.3 and 79.5 m² g⁻¹. The results demonstrate the pore size reduces and the BET surface area increases with the Ce addition. Meanwhile, the pore size and the specific surface area have linear relation with bulk Ce content, respectively (Fig. S2). Hence, it can be conclude that the addition of Ce has obvious influence on the structure of the Ce_aMnO_x samples, also confirming the strong interaction between Mn and Ce.

3.3. SEM images

SEM images of the samples are shown in Fig. 3. The morphology of MnO_x presents microsphere like arbutus (Fig. 3(a) and (b)) possessing lots of doming on the surface of MnO_x and the size of about 800 nm. Both $\text{Ce}_{0.02}\text{MnO}_x$ and $\text{Ce}_{0.03}\text{MnO}_x$ show the arbutus-like microspheres and the size is 500 and 430 nm, respectively. Furthermore, both $\text{Ce}_{0.04}\text{MnO}_x$ and $\text{Ce}_{0.05}\text{MnO}_x$ are hollow shell structure with open mouth and the size reduces to 370 and 350 nm, respectively. This phenomenon may be because the strong interaction between Mn and

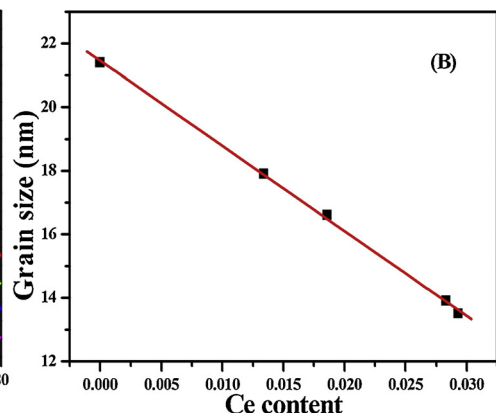


Fig. 1. (A) XRD patterns of MnO_x (a), $\text{Ce}_{0.02}\text{MnO}_x$ (b), $\text{Ce}_{0.03}\text{MnO}_x$ (c), $\text{Ce}_{0.04}\text{MnO}_x$ (d) and $\text{Ce}_{0.05}\text{MnO}_x$ (e) and (B) crystal size with different Ce content.

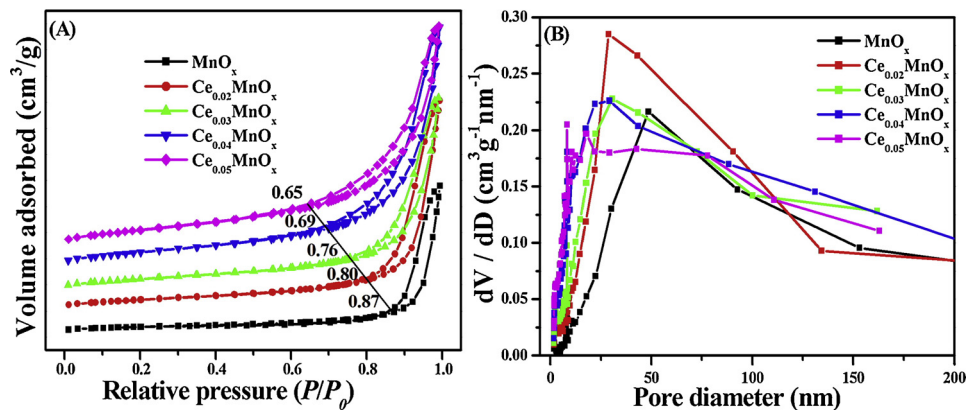


Fig. 2. N_2 adsorption-desorption isotherms (A) and the pore size distribution (B) of Ce_aMnO_x .

Ce, which hindered the further assembly of Ce_aMnO_x crystal, and result in the smaller crystal size and hollow shell structure with open mouth.

3.4. TEM images

The TEM images of MnO_x (Fig. 4(a)–(c)), $Ce_{0.02}MnO_x$ (Fig. 4(d)–(f)) and $Ce_{0.03}MnO_x$ (Fig. 4(g)–(i)) are presented in Fig. 4. It can be seen that all samples are hierarchical structure assembled by particles. The average particle sizes of MnO_x , $Ce_{0.02}MnO_x$ and $Ce_{0.03}MnO_x$ is about 21, 18 and 17 nm, respectively, which is agreement with the results of XRD (Table 1). In the HRTEM image of MnO_x (Fig. 4c), the lattice fringes are clear and demonstrate the (211) and (222) planes corresponding to the phase bixbyite Mn_2O_3 . The lattice stripes of $Ce_{0.02}MnO_x$ are not obvious, but the lattice stripes of (211) and (222) still can be observed in Fig. 4(f). However, the lattice fringes of the $Ce_{0.03}MnO_x$ (Fig. 4i) are unclear due to the much weaker crystallinity and it is consistent with the XRD results, confirming the decrease in the crystallinity of $Ce_{0.03}MnO_x$. In addition, defects can be clearly seen at the junction of particles in the HRTEM image of Ce_aMnO_x , suggesting that hierarchical structure can cause more defects derived from the Ce addition [45].

3.5. H_2 -TPR analysis

The oxidation and reduction behavior of the catalysts is analyzed by H_2 -TPR displayed in Fig. 5. For MnO_x , three H_2 consumption peaks in the range of 163–238, 238–327 and 327–420 °C are detected. The peak in the range of 163–238 °C is ascribed to the reduction of surface adsorbed oxygen species. The peaks in the range of 238–327 and

327–420 °C belong to the reduction of MnO_2/Mn_2O_3 to Mn_3O_4 and Mn_3O_4 to MnO , respectively [46–48]. For Ce_aMnO_x , the three reduction peaks are still observed. The reduction peak in the range of 75–300 °C is magnified and shown in the left of Fig. 5. It is noticed that the initial reduction temperature decrease gradually, the peak broadens and the intensity increases gradually with the increase of the Ce content. This indicates that there is more abundance of surface adsorbed oxygen species on Ce_aMnO_x , which is also confirmed by the O_2 -TPD results displayed in Fig. S3. In addition, compared with MnO_x , the second reduction peak belongs to the reduction of MnO_2/Mn_2O_3 to Mn_3O_4 shifts slightly to the high temperature. Moreover, it can be seen that the third peak also shifts to high temperature with increasing the Ce content, but the peak shift to low temperature when the Ce content is more than 3%. The above results suggest the existence of the strong interaction between Ce and Mn oxides in Ce_aMnO_x [49], which is closely related to the outstanding redox capacity of MnO_x [50] and strong store and release oxygen of Ce oxide [51].

3.6. XPS study

The XPS is used to analyze the surface information including the surface atomic concentration and chemical states of the elements. The results are depicted in Fig. 6.

The Mn2p spectra of MnO_x and Ce_aMnO_x are fitted three main spin-orbital lines at 640.45, 641.65 and 642.9 eV (Fig. 6A), which are ascribed to the Mn^{2+} , Mn^{3+} and Mn^{4+} species, respectively [15,52]. The percentage of these species is calculated by the area ratio, and the results are listed in Table 2. The percentage of Mn^{4+} (Mn^{4+} to (Mn^{4+} +

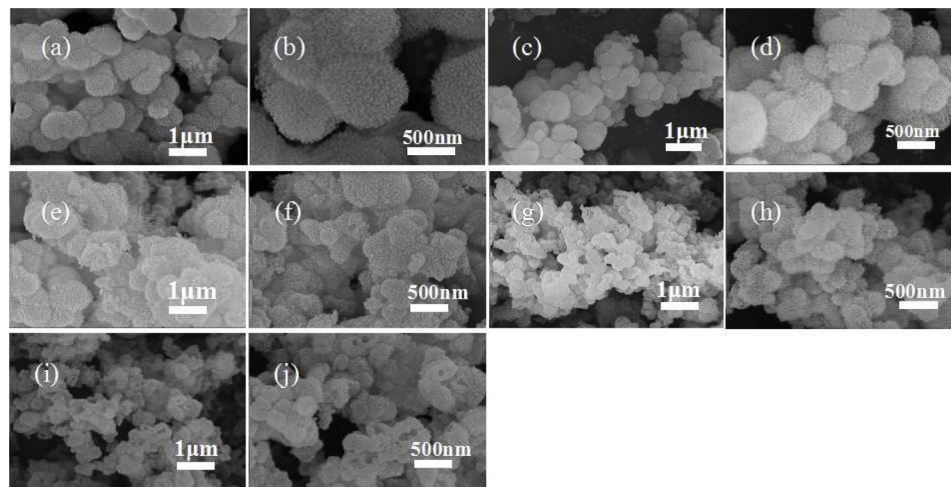


Fig. 3. SEM images of MnO_x (a and b), $Ce_{0.02}MnO_x$ (c and d), $Ce_{0.03}MnO_x$ (e and f), $Ce_{0.04}MnO_x$ (g and h), $Ce_{0.05}MnO_x$ (i and j).

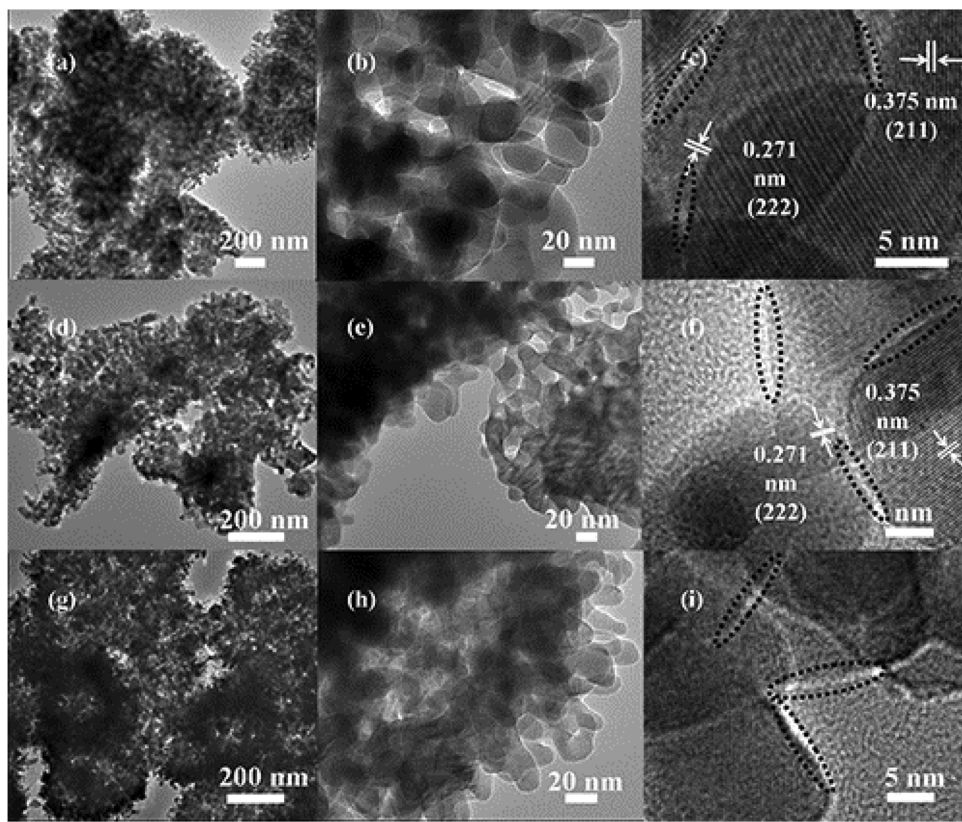


Fig. 4. TEM images of MnO_x (a, b and c), $\text{Ce}_{0.02}\text{MnO}_x$ (d, e and f) and $\text{Ce}_{0.03}\text{MnO}_x$ (g, h and i).

$(\text{Mn}^{3+} + \text{Mn}^{2+})$) is 27.2%, 33.6%, 34.9%, 32.8% and 31.4% over MnO_x , $\text{Ce}_{0.02}\text{MnO}_x$, $\text{Ce}_{0.03}\text{MnO}_x$, $\text{Ce}_{0.04}\text{MnO}_x$ and $\text{Ce}_{0.05}\text{MnO}_x$, respectively. It is observed that the percentage of Mn^{4+} on Ce_aMnO_x is more than that on MnO_x , moreover, the change of the Mn^{4+} content presents volcano type with the increase of the Ce content (Fig. S4(A)). It is worth mentioning that $\text{Ce}_{0.03}\text{MnO}_x$ has the highest Mn^{4+} content (34.9%) among the Ce_aMnO_x samples. The results indicate that the addition of Ce can improve the formation of the surface Mn^{4+} species, and the incorporation of moderate Ce leads to the most amount of the surface Mn^{4+} species.

For the Ce3d spectra (Fig. 6B), eight peaks can be fitted by deconvolution according to the literatures [53,54]. The peaks at 881.7, 887.5, 897.4, 900.2, 906.9 and 916.3 eV denoted as V, V'', V''', U, U'' and U'''

are attributed to the Ce^{4+} species, and the peaks at 883.3 and 903.5 eV are assigned to the Ce^{3+} species which are denoted as V' and U'. The calculated results of the correlative Ce^{4+} and Ce^{3+} percentage based on the peaks area are listed in Table 2. It is noteworthy that the ratio of Ce^{3+} to $(\text{Ce}^{4+} + \text{Ce}^{3+})$ (Ce^{3+}/Ce) is 21.7%, 23.7%, 20.1% and 18.5% for $\text{Ce}_{0.02}\text{MnO}_x$, $\text{Ce}_{0.03}\text{MnO}_x$, $\text{Ce}_{0.04}\text{MnO}_x$ and $\text{Ce}_{0.05}\text{MnO}_x$, respectively, which indicate that the proportion of Ce^{3+}/Ce increases with the Ce content, and then decreases gradually. In other words, there is a volcanic type relation between the surface Ce^{3+}/Ce ratio and the Ce content in Ce_aMnO_x (Fig. S4(B)). Meanwhile, the surface Ce^{3+} amount of the $\text{Ce}_{0.03}\text{MnO}_x$ catalyst is higher than that of the others.

Interestingly, combined the XPS results of Mn and Ce, it is found that there is a linear relation between the surface Mn^{4+}/Mn ratio and

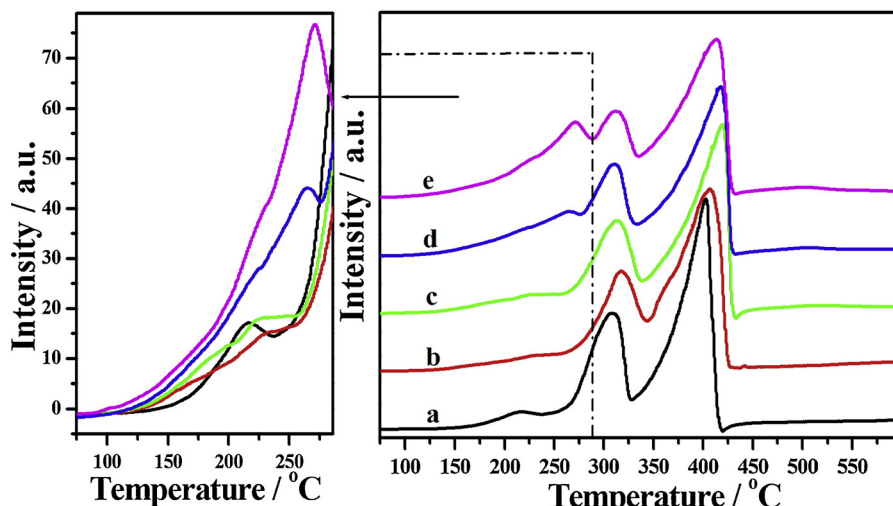


Fig. 5. H_2 -TPR profiles of MnO_x (a), $\text{Ce}_{0.02}\text{MnO}_x$ (b), $\text{Ce}_{0.03}\text{MnO}_x$ (c), $\text{Ce}_{0.04}\text{MnO}_x$ (d) and $\text{Ce}_{0.05}\text{MnO}_x$ (e).

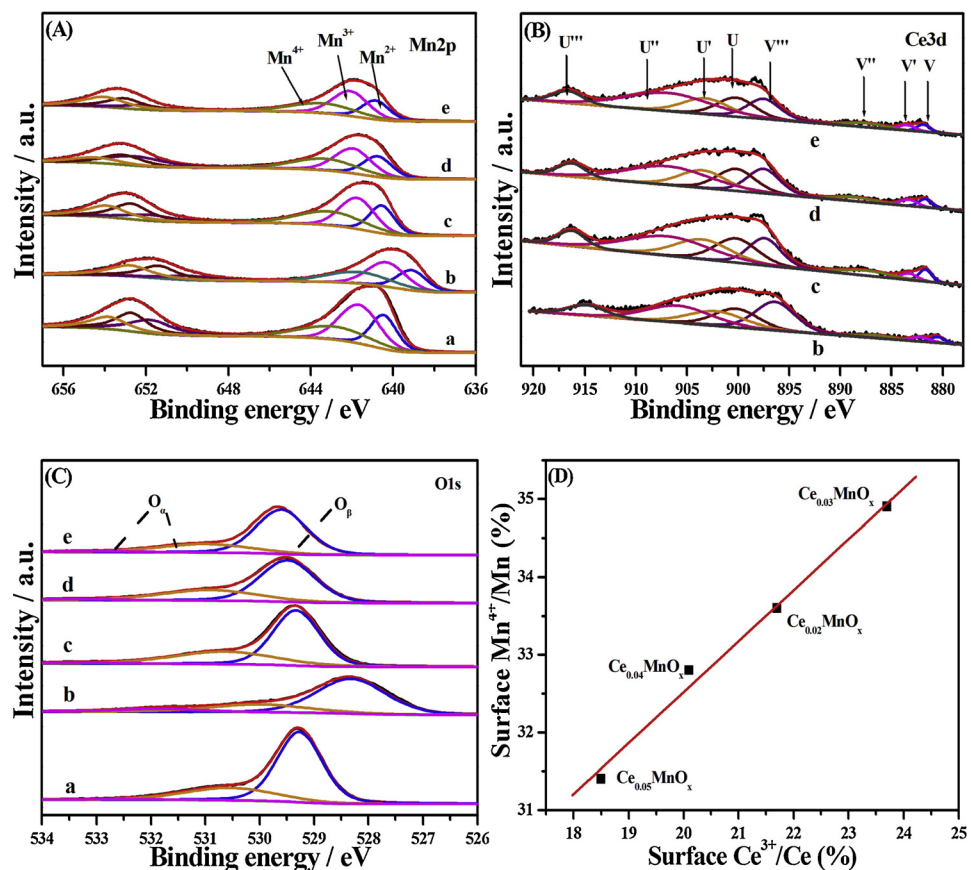


Fig. 6. XPS for (A) Mn2p, (B) Ce 3d, (C) O 1s of MnO_x (a), $\text{Ce}_{0.02}\text{MnO}_x$ (b), $\text{Ce}_{0.03}\text{MnO}_x$ (c), $\text{Ce}_{0.04}\text{MnO}_x$ (d) and $\text{Ce}_{0.05}\text{MnO}_x$ (e), (D) relation between surface Mn^{4+}/Mn and surface Ce^{3+}/Ce of Ce_aMnO_x .

the surface Ce^{3+}/Ce ratio (Fig. 6D). Thus, it is suggested that the addition of Ce in Ce_aMnO_x may be cause the oxidation reduction cycle like $\text{Mn}^{3+} + \text{Ce}^{4+} \leftrightarrow \text{Mn}^{4+} + \text{Ce}^{3+}$ [55,56], confirming the strong interaction between Ce and Mn. That is to say, it is favor of producing more amounts of the surface Mn^{4+} and Ce^{3+} species accompanied by moderate Ce content in the $\text{Ce}_{0.03}\text{MnO}_x$ catalysts.

As displayed in Fig. 6C, the XPS of O 1s can be fitted into three peaks, the low binding energy peak at 528.5–529.8 eV is attributed to the lattice oxygen (O_β). Two shoulder peaks at 531.9–533.1 and 530.1–531.3 eV are ascribed to the chemisorbed water and the surface adsorbed oxygen (O_α) such as O_2^{2-} , O_- , a part of defect oxide or hydroxyl-like groups, respectively [16,43,54,57]. With the increase of Ce content, the O_α content ($\text{O}_\alpha/(\text{O}_\alpha + \text{O}_\beta)$) also increases gradually, which is compliance with the results of $\text{H}_2\text{-TPR}$ and $\text{O}_2\text{-TPD}$. It may be because of strong interaction between Ce and Mn (Table 2).

From the above XPS results, a small amount of Ce doping can reduce the content of the surface Mn^{3+} , and increase the content of surface

Mn^{4+} , Ce^{3+} and O_α species. This indicates that Ce doping can result in the redox reaction between Ce^{4+} and Mn^{3+} to produce the more amounts of Mn^{4+} species. The presence of Ce^{3+} may lead to the charge imbalance than can form oxygen vacancies and unsaturated chemical bonds on the surface of catalyst. In other words, this situation will generate more additional chemisorbed oxygen or weakly adsorbed oxygen species on the surface of the Ce_aMnO_x catalysts and the chemisorbed oxygen is more reactive than the lattice oxygen due to its much higher mobility [55].

Another interesting finding is that the surface and bulk atomic concentration of Ce and Mn are different obviously based on the detected results of XRF and XPS. According to the XRF results, the atomic ratio of Ce to Mn (Ce/Mn) in bulk is 0.014, 0.019, 0.029 and 0.030 for $\text{Ce}_{0.02}\text{MnO}_x$, $\text{Ce}_{0.03}\text{MnO}_x$, $\text{Ce}_{0.04}\text{MnO}_x$ and $\text{Ce}_{0.05}\text{MnO}_x$, respectively. Nevertheless, the corresponding Ce/Mn atomic ratios on surface of these samples are 0.15, 0.16, 0.18 and 0.19, which are much higher than those in the bulk Ce_aMnO_x . These results confirm that a large

Table 2
XPS data and activity results of the MnO_x and Ce_aMnO_x catalysts.

Catalysts	O (%)	Mn (%)	Ce (%)	Ce/Mn ^a	Mn^{4+}/Mn ^b (%)	O_α/O ^c (%)	Ce^{3+}/Ce ^d (%)	T_{50} (°C)	T_{100} (°C)	E_a (kJ/mol)
MnO_x	58.3	41.7	–	–	27.2	29	–	241	251	155.2
$\text{Ce}_{0.02}\text{MnO}_x$	58.9	35.8	5.3	0.148	33.6	33.9	21.7	221	230	98.0
$\text{Ce}_{0.03}\text{MnO}_x$	57.8	36.5	5.7	0.156	34.9	34.9	23.7	215	225	90.4
$\text{Ce}_{0.04}\text{MnO}_x$	56.2	37.2	6.6	0.177	32.8	36.2	20.1	225	235	91.5
$\text{Ce}_{0.05}\text{MnO}_x$	56.3	36.6	7.1	0.194	31.4	40.0	18.5	227	235	104.3

^a The element content is measured by the XPS analysis.

^b The ratio of surface Mn^{4+} to $(\text{Mn}^{4+} + \text{Mn}^{3+} + \text{Mn}^{2+})$.

^c The ratio of surface Ce^{3+} to $(\text{Ce}^{4+} + \text{Ce}^{3+})$.

^d The ratio of surface O_α to $(\text{O}_\alpha + \text{O}_\beta)$.

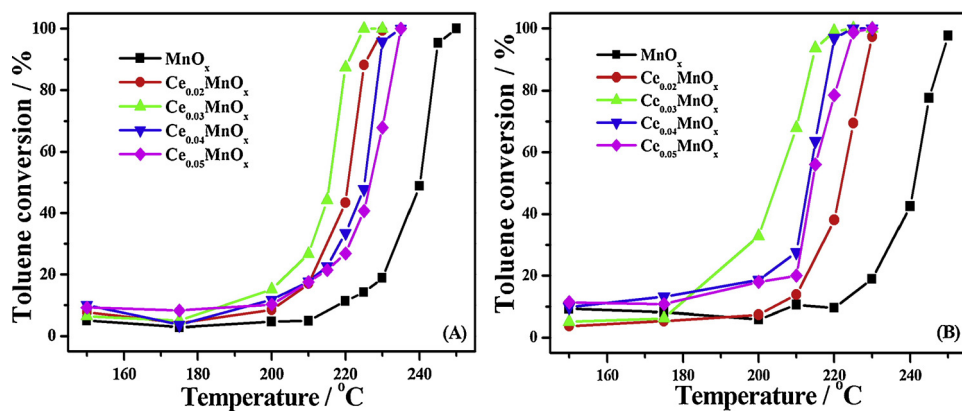


Fig. 7. Catalytic performance of toluene oxidation over the MnO_x and Ce_aMnO_x catalysts, (A) without H₂O and (B) with H₂O. [Reaction conditions: [C₇H₈] = 1000 ppm, [O₂] = 20%, and N₂ balance].

proportion of Ce should be dispersed on the surface of the Ce_aMnO_x samples. Ce oxide package on the surface of the Ce_aMnO_x particle after adding Ce to MnO_x. There is a strong interaction between Ce and Mn by an oxidation reduction cycle of Mn³⁺ + Ce⁴⁺ ⇌ Mn⁴⁺ + Ce³⁺. And the interaction not only causes the crystal size decrease gradually, but also hinders to the further growth of Ce_aMnO_x. In other word, the strong interaction between Ce and Mn leads to the morphology change of Ce_aMnO_x. The influences of the strong interaction between Mn and Ce on the formation of the hollow shells with open mouths in Ce_{0.04}MnO_x and Ce_{0.05}MnO_x. Ce need to be investigated systematically by a lot of experiments in our future work.

3.7. Catalytic activity

The catalytic activities of the Ce_aMnO_x samples are investigated by using catalytic toluene combustion as model reaction. CO, benzaldehyde and benzoic acid etc. were not detected except CO₂ and H₂O in our experiment condition [38,47,58]. Fig. 7(A) displays the conversion of toluene as function of the reaction temperature. For the MnO_x catalyst, it is observed that the toluene conversion is less than 5% below 210 °C. And then the toluene conversion gradually rises with the increase of reaction temperature, and increases rapidly when the reaction temperature is above 230 °C. Especially, the temperature at the toluene conversion of 50% (T₅₀) and 100% (T₁₀₀) is 240 and 250 °C, respectively. For Ce_aMnO_x, T₅₀ is 221, 215, 225 and 227 °C over the Ce_{0.02}MnO_x, Ce_{0.03}MnO_x, Ce_{0.04}MnO_x and Ce_{0.05}MnO_x catalysts, respectively, corresponding the T₁₀₀ is 230, 225, 235 and 235 °C. Obviously, catalytic performance of Ce_aMnO_x is higher than that of MnO_x. The results suggest that addition of Ce could increase combustion efficiency of toluene compared with MnO_x. Meanwhile, it is quite clear that the Ce_{0.03}MnO_x catalyst exhibits the best catalytic performance for toluene combustion. Besides, the T₅₀ and T₁₀₀ for Ce_{0.03}MnO_x are 25 °C lower than those of MnO_x. The above results indicate that there is also a striking improvement of catalytic toluene combustion while adding a small amount of Ce to MnO_x, however, doping more Ce can lead to the decrease of the activity. Thus, the Ce_{0.03}MnO_x catalyst shows superior catalytic property for the toluene combustion, which is associated with the proper Ce content. Moreover, the O₂-TPSR results also confirm that only CO₂ and H₂O and no other products are detected over Ce_{0.03}MnO_x in Fig. S5, indicating that Ce_{0.03}MnO_x shows outstanding deep oxidation activity, which is consistent with the result of literatures [38,47,59].

In order to investigate the effect of H₂O on the catalytic activity, 5% of H₂O is introduced into the feed during the test, and the results are displayed in the Fig. 7(B). As shown in Figure, T₅₀ is 240, 220, 205, 213, 214 °C over MnO_x, Ce_{0.02}MnO_x, Ce_{0.03}MnO_x, Ce_{0.04}MnO_x and Ce_{0.05}MnO_x catalysts, respectively, and corresponding T₁₀₀ is 250, 235,

220, 225, 230 °C. It is found that the toluene conversion with H₂O slightly decrease compared with that without H₂O over MnO_x and Ce_{0.02}MnO_x. However, it is noteworthy that the toluene conversion with H₂O is much higher than that without H₂O for the Ce_{0.03}MnO_x, Ce_{0.04}MnO_x, and Ce_{0.05}MnO_x catalysts at the same reaction temperature. It can be concluded that the catalytic activities are improved after the addition of 5 vol.% H₂O over the Ce_{0.03}MnO_x, Ce_{0.04}MnO_x, and Ce_{0.05}MnO_x catalysts.

The dynamics parameters are calculated under the conversion of less than 30% (Fig. S6). As shown in the Table 2, the apparent activation energy (Ea) obtained from Arrhenius plots is 155.2, 98.0, 90.4, 91.5 and 104.3 kJ·mol⁻¹ for MnO_x, Ce_{0.02}MnO_x, Ce_{0.03}MnO_x, Ce_{0.04}MnO_x and Ce_{0.05}MnO_x, respectively. The Ea values over Ce_aMnO_x are much lower than that over MnO_x, meanwhile, the Ea value of Ce_{0.03}MnO_x is the lowest among these Ce_aMnO_x catalysts, which is in good consistent with the results of catalytic activity.

Turnover number (TON), a fundamental measurement for catalytic reaction, refers to reaction cycles occurring on each active site over a period of time (1 min). The TON values on the basis of surface Mn content are calculated over the Ce_aMnO_x samples under both without H₂O and with H₂O at 200 and 220 °C. The results are displayed in Fig. 8. Ce_{0.03}MnO_x exhibits the highest TON value at both 200 and 220 °C under the feed without H₂O among these Ce_aMnO_x catalysts. It is noteworthy that the TON value changes a lot when H₂O is added to the reaction feed. In general, the TON values decrease slightly for the MnO_x and Ce_{0.02}MnO_x catalysts compare with those without H₂O. But the TON values are enhanced significantly with H₂O for the Ce_{0.03}MnO_x, Ce_{0.04}MnO_x and Ce_{0.05}MnO_x catalysts. The TONs follow as the order: Ce_{0.03}MnO_x > Ce_{0.04}MnO_x > Ce_{0.05}MnO_x > Ce_{0.02}MnO_x > MnO_x, which coincide with the catalytic activity. The results show that the addition of Ce can improve the catalytic performance of the catalyst under the condition of H₂O supply. To sum up, the Ce_{0.03}MnO_x catalyst possesses the highest TON value whether low or high conversion of toluene, so the Ce_{0.03}MnO_x catalyst displays the best catalytic ability for toluene combustion.

3.8. Stability test and effect of WHSV

Normally, the industrial VOCs emission contains water, so the stability test with H₂O must be considered. The test is evaluated over the Ce_{0.03}MnO_x catalyst under condition of 20,000 mL·g⁻¹ h⁻¹ at 240 °C. It can be seen from Fig. S7 that 100% toluene conversion is almost unchanged for 5 h when 5 vol.% H₂O is added in the feed. Moreover, the effect of 10 vol.% H₂O on toluene conversion is also negligible. When water content is increased to 20 vol.%, the toluene conversion decreases to about 96%. However, the conversion could restore to about 99% after removing the water vapor from the feed. From these results, it can

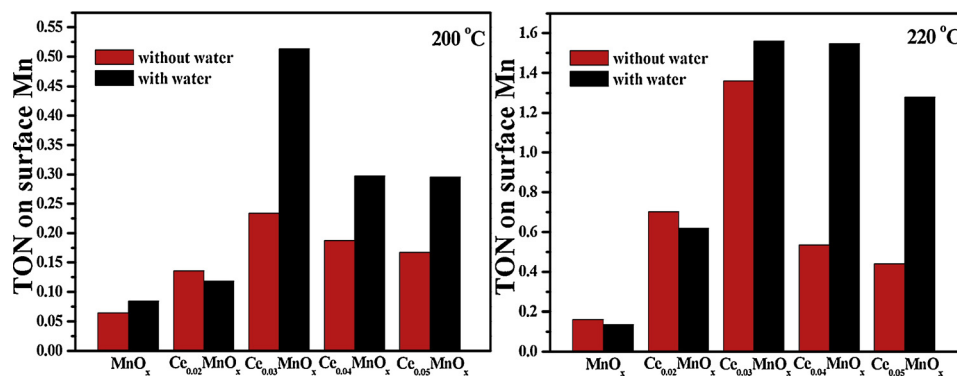


Fig. 8. TONs based on the surface Mn species over the Ce_aMnO_x catalysts at 200 and 220 °C.

be concluded that the Ce_{0.03}MnO_x catalyst still displays a great performance even under a mass of water vapor.

The stability test without H₂O is also performed under condition of 20,000 mL·g⁻¹ h⁻¹ at 240 °C over Ce_{0.03}MnO_x due to its especial activity. As displayed in the Fig. S8(A), the toluene conversion remains unchanged (100%) for 60 h. Meanwhile, the toluene oxidation for three successive runs over Ce_{0.03}MnO_x is displayed in Fig. S8(B). It can be seen that T₅₀ is 215, 219 and 221 °C over the Ce_{0.03}MnO_x catalyst for 1st, 2nd and 3rd run, respectively, corresponding the T₁₀₀ is 225, 225 and 226 °C, suggesting there is no obvious difference among the three successive runs. To sum up, the Ce_{0.03}MnO_x catalyst has good activity stability and it is crucial for practical application.

The effect of WHSV on toluene oxidation is also regarded as a key parameter. The toluene conversion over the Ce_{0.03}MnO_x catalyst under different WHSV of 20,000, 40,000 and 80,000 mL·g⁻¹ h⁻¹ is demonstrated in Fig. S9. When the WHSV is 40,000 mL·g⁻¹ h⁻¹, the T₅₀ and T₁₀₀ are 228 and 240 °C, respectively, which are only 12 and 15 °C higher than those under 20,000 mL·g⁻¹ h⁻¹. Similarly, when the WHSV increases to 80,000 mL·g⁻¹ h⁻¹, the T₅₀ and T₁₀₀ increase 19 and 29 °C compared with the corresponding results at 20,000 mL·g⁻¹ h⁻¹. Thus, the results indicate that the Ce_{0.03}MnO_x catalyst exhibits much better catalytic toluene combustion performance even under much higher WHSV.

3.9. In situ DRIFTS study

In order to study the surface adsorbed species and understand the catalytic reaction process of toluene combustion, the *in situ* DRIFTS experiments were performed over the MnO_x and Ce_{0.03}MnO_x catalysts.

Fig. 9 displays the DRIFTS of MnO_x(A) and Ce_{0.03}MnO_x(B) after being exposed to toluene + N₂ at 220 °C with different time interval. It can be seen that there is no characteristic peak at first 5 min on MnO_x (Fig. 10(A)). And after 5 min, five absorption peaks are detected, and the peaks intensities gradually increase with extended time and unchanged till 50 min. The peak at 1329 cm⁻¹ is attributed to the skeletal C–C stretching vibration for benzaldehyde, and the bands at 1650 and 1693 cm⁻¹ are ascribed to the C=O stretching vibration of aldehydic. Furthermore, the peaks at 1404 and 1525 cm⁻¹ belong to the symmetric C–O stretching vibration and antisymmetric C–O stretching vibration of benzoate, respectively [60]. For Ce_{0.03}MnO_x (Fig. 9(B)), the peaks are observed obviously after 2 min, and the peaks intensity increases significantly reaching saturation after about 20 min. The bands at 1404, 1445 and 1534 cm⁻¹ are ascribed to symmetric C–O stretching vibration of benzoate, skeletal C–C stretching vibration of benzoate and antisymmetric C–O stretching vibration of benzoate, respectively. And the bands at 1551 and 1592 cm⁻¹ are attributed to skeletal C–C stretching vibration of the aromatic ring. The band at 3069 cm⁻¹ is assigned to phenyl C–H stretching vibration of aromatic ring [60–62]. It is noteworthy that the peaks belong to the benzaldehyde are not observed. Interestingly, the benzaldehyde and benzoic acid species are

formed on the MnO_x catalyst after absorbing toluene, while only benzoic acid is detected on the surface of the Ce_{0.03}MnO_x catalyst. These results indicate toluene can be rapidly adsorbed and activated to the adsorbed benzoic acid species than the benzaldehyde species on the Ce_{0.03}MnO_x catalyst, suggesting the strong oxidation ability of the Ce_{0.03}MnO_x catalyst.

After the adsorption of toluene, 20% O₂+N₂ is added into the IR cell at 220 °C. For MnO_x (Fig. 9(C)), it's worth noting that the peaks at 1650 and 1693 cm⁻¹ assign to benzaldehy clearly decrease and the peak at 1525 cm⁻¹ assign to benzoate slightly decrease after 40 min, which is attributed to the partial oxidation of the benzaldehyde species to benzoate in the process. It can be concluded that toluene could be absorbed on the MnO_x catalyst and oxidated to aldehydic, then to benzaldehyde. For Ce_{0.03}MnO_x (Fig. 9(D)), the peaks intensities clearly decrease at 10 min and only much weaker bands can be observed after 30 min. On the basis of these results, it can be concluded that the toluene could be oxidized to benzoate and to CO₂ subsequently [63]. The above results demonstrate toluene can be oxidized more quickly over Ce_{0.03}MnO_x than over MnO_x, which may be the main factor of excellent performance over the Ce_{0.03}MnO_x catalyst.

Furthermore, in order to understand the effect of H₂O on the toluene oxidation, *in situ* DRIFTS tests of the toluene adsorption and reaction at 210 °C are carried out over Ce_{0.03}MnO_x based on the lower toluene conversion in activity evaluation under the condition with H₂O and without H₂O. The results are given in Fig. 10. The characteristic peaks of the toluene adsorption 210 °C are the same as those at 220 °C (Fig. 10(A)). It is noticed that the characteristic peaks almost disappear completely after introducing O₂/N₂ without H₂O for 80 min. However, when the O₂/N₂ with H₂O is introduced to the IR cell, the characteristic peaks nearly disappear after 40 min (Fig. 10(B)). Combined the above results, the introduction of water is beneficial to the catalytic reaction of toluene oxidation, which is consistent with the result of toluene conversion.

In addition, the experiments of temperature programmed desorption of toluene (Toluene TPD) also confirm above results. Toluene TPD is performed over the Ce_{0.03}MnO_x catalyst with different adsorption conditions. As shown in Fig. S10, only CO₂ desorption peak is detected without CO and toluene etc. For the toluene adsorption, the CO₂ desorption peak is observed at about 307 °C. When the toluene and O₂ are co-adsorbed on the Ce_{0.03}MnO_x catalyst, the CO₂ desorption peak is no significant difference with the result of pure toluene, but the peak intensities increase a lot, meaning O₂ could promote the adsorption of toluene. Furthermore, when the O₂, H₂O and toluene are co-adsorbed on Ce_{0.03}MnO_x, the temperature of the CO₂ desorption peak decreases obviously (about 274 °C), the results suggest the co-adsorption of O₂/H₂O promote the reaction of toluene. In other words, the addition of water can promote the adsorption and activation of toluene. Thus, according to the literatures [63,64], we think the introduction of water promotes the adsorption and activation of toluene and oxygen leading to the much better activity of toluene combustion over the

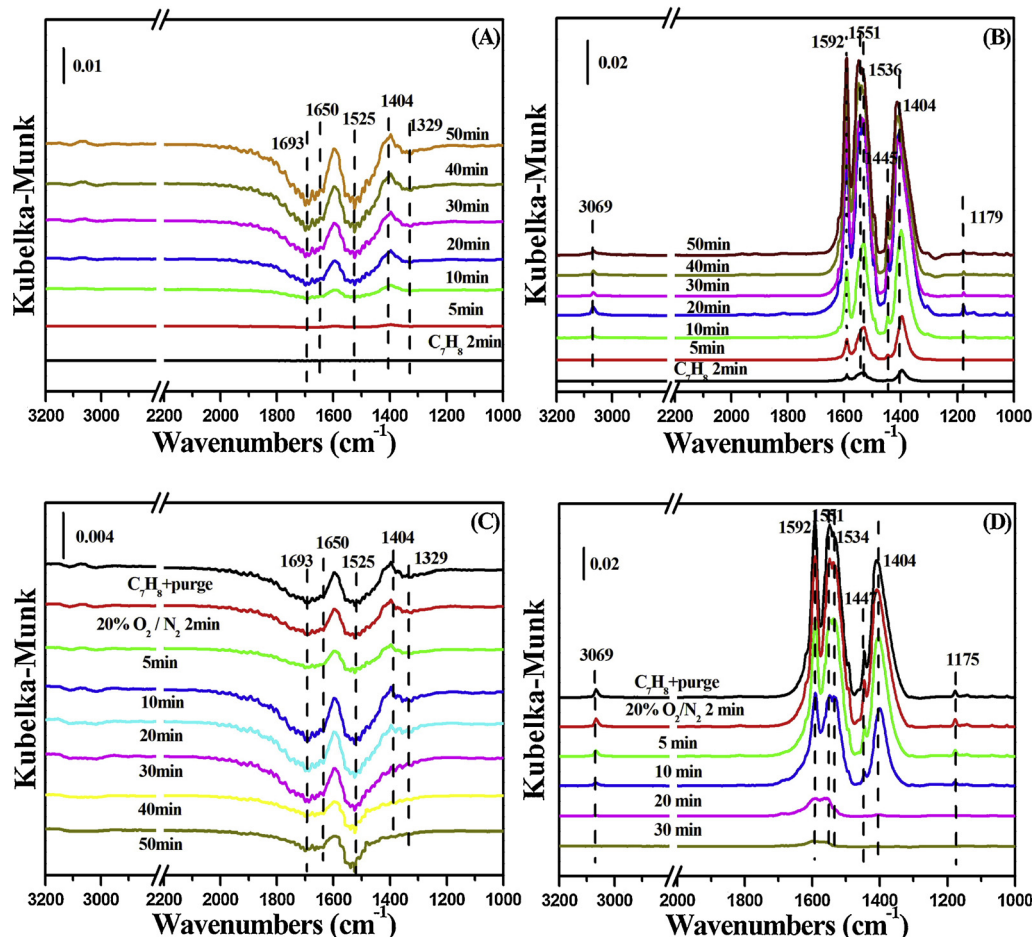


Fig. 9. *In situ* DRIFTS of toluene adsorption for different time over MnO_x (A) and $\text{Ce}_{0.03}\text{MnO}_x$ (B); after inputting 20% O_2/N_2 over MnO_x (C) and $\text{Ce}_{0.03}\text{MnO}_x$ (D) at 220 °C.

$\text{Ce}_{0.03}\text{MnO}_x$ catalyst. It is reported that the introduce of H_2O can lead to the appearance of hydroperoxyl-like, which is benefit of the activation O–O bond, enhancing the catalyst activity of toluene oxidation [64,65]. A detailed study on the role of H_2O needs to be carried out in the future.

3.10. Effect of Ce

To sum up, doping of Ce could efficiently promote the toluene

combustion activity of the Ce_aMnO_x catalysts, meanwhile, the $\text{Ce}_{0.03}\text{MnO}_x$ catalyst reveals the best activity among these catalysts. According to the results of various characterizations, it can be concluded that there is strong interaction between Ce and Mn, which improve the formation of more surface adsorbed oxygen and surface Mn^{4+} species that are favor of the adsorption and activation of toluene.

Compared the Ce/Mn atomic ratio in bulk with on surface, it is obvious that the Ce/Mn ratio on the surface of Ce_aMnO_x is much higher than that in bulk of the catalysts. It indicates the Ce mainly disperses on

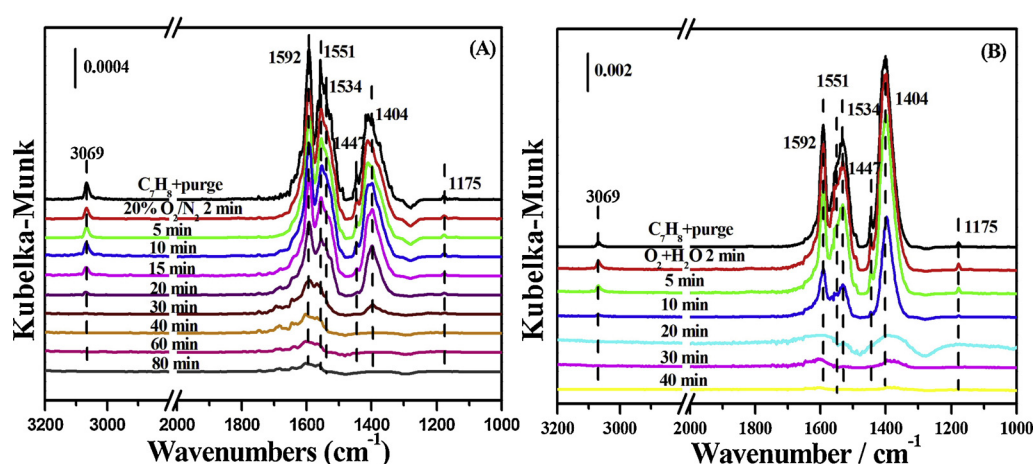


Fig. 10. *In situ* DRIFTS under 20% O_2/N_2 (A) and 20% O_2/N_2 with H_2O over $\text{Ce}_{0.03}\text{MnO}_x$ catalyst before pre-adsorbed toluene at 210 °C.

the surface of Ce_aMnO_x , which result in the smaller particle sizes verified by XRD and TEM. Moreover, the strong interaction between Ce and Mn hinders the further increase of the Ce_aMnO_x particles to form the microsphere structure smaller hollow shell structure with open mouth, leading to much higher BET surface area. This is due to the strong interaction between Mn and Ce which is confirmed by XRD and Raman. Besides, there are more defects formed after doping Ce element verified by TEM. XPS results also prove that the introduction of the Ce not only lead to produce more of the chemical adsorption oxygen species on the catalyst, but also can form more surface Mn^{4+} species by the reaction ($\text{Mn}^{3+} + \text{Ce}^{4+} \leftrightarrow \text{Mn}^{4+} + \text{Ce}^{3+}$) [55,56], which contribute to the activity of toluene oxidation. However, when too much Ce is added for $\text{Ce}_{0.05}\text{MnO}_x$, Ce oxide covers the surface of Ce_aMnO_x , thus reducing the active sites on the surface of the catalyst and weakening the activity. So the $\text{Ce}_{0.03}\text{MnO}_x$ catalyst exhibits the best catalytic activity, much better thermal stability and water resistance among the Ce_aMnO_x catalysts even under the WHSV of $80,000 \text{ mL g}^{-1} \text{ h}^{-1}$.

Furthermore, the *in situ* DRIFTS prove that the adsorption speed and amount of toluene are much faster and more on the $\text{Ce}_{0.03}\text{MnO}_x$ catalyst than those on the MnO_x catalyst. Especially, toluene could be activated directly to form benzoic acid over $\text{Ce}_{0.03}\text{MnO}_x$ catalyst than benzaldehyde and benzoic acid on MnO_x . Moreover, the benzoic acid species over $\text{Ce}_{0.03}\text{MnO}_x$ catalyst can be oxidized quickly to CO_2 . Therefore, Ce addition can enhance the oxidation ability and improve adsorption and activation of toluene for $\text{Ce}_{0.03}\text{MnO}_x$.

4. Conclusion

In this work, a series of hollow hierarchical structure Ce_aMnO_x materials like arbutus are prepared by redox co-precipitation method for catalytic toluene combustion. The various characterization results verify the strong interaction between Ce and Mn lead to the changes in the morphology of catalysts and form more defects with the Ce addition. Therefore, there are more surface adsorption oxygen and the surface Mn^{4+} species on Ce_aMnO_x compared with MnO_x . Among these Ce_aMnO_x catalysts, $\text{Ce}_{0.03}\text{MnO}_x$ exhibits the optimum catalytic performance that the T_{50} and T_{100} are 25°C lower than those of MnO_x as well as much higher stability and H_2O resistance due to the abundant surface oxygen and Mn^{4+} species. Especially, the introduction of H_2O in the feed enhances the catalytic activity over $\text{Ce}_{0.03}\text{MnO}_x$, which may be related to the improvement of toluene adsorption and oxygen activation by H_2O . Furthermore, the reaction process investigation indicates that toluene can be rapidly adsorbed and activated to form the benzoic acid species without benzaldehyde on the surface of $\text{Ce}_{0.03}\text{MnO}_x$, and then is oxidized quickly to CO_2 compared with MnO_x . This also explains why $\text{Ce}_{0.03}\text{MnO}_x$ has better catalytic activity.

Acknowledgements

This work is supported by Harbin science and technology innovation talent fund (Outstanding academic leader project) (RC2016XK015004), the Innovative Research Project of Key Laboratory of Functional Inorganic Material Chemistry (Heilongjiang University), Ministry of Education (2015).

Appendix A. Supplementary data

Supplementary material related to this article can be found, in the online version, at doi:<https://doi.org/10.1016/j.apcatb.2019.01.005>.

References

- [1] L.F. Liotta, Catalytic oxidation of volatile organic compounds on supported noble metals, *Appl. Catal. B: Environ.* 100 (2010) 403–412.
- [2] M.A. Bari, W.B. Kindzierski, Ambient volatile organic compounds (VOCs) in Calgary, Alberta: sources and screening health risk assessment, *Sci. Total Environ.* 631–632 (2018) 627–640.
- [3] J.V. Durme, J. Dewulf, W. Sysmans, C. Leys, H.V. Langenhove, Abatement and degradation pathways of toluene in indoor air by positive corona discharge, *Chemosphere* 68 (2007) 1821–1829.
- [4] V. Héqueta, C. Raillard, O. Debono, F. Thévenet, N. Locoge, L. Le Coq, Photocatalytic oxidation of VOCs at ppb level using a closed-loop reactor: the mixture effect, *Appl. Catal. B: Environ.* 226 (2018) 473–486.
- [5] L. Chen, J. Tang, L. Song, P. Chen, J. He, C. Au, S. Yin, Heterogeneous photocatalysis for selective oxidation of alcohols and hydrocarbons, *Appl. Catal. B: Environ.* 242 (2019) 379–388.
- [6] B. Yang, Z. Fu, A. Su, J. She, M. Chen, S. Tang, W. Hu, C. Zhang, Y. Liu, Influence of tetraalkylammonium cations on quality of decatungstate and its photocatalytic property in visible light-triggered selective oxidation of organic compounds by dioxygen, *Appl. Catal. B: Environ.* 242 (2019) 249–257.
- [7] C.J. Hennigan, M.M.H. El-Sayed, A. Hodzic, Detailed characterization of a mist chamber for the collection of watersoluble organic gases, *Atmos. Environ.* 188 (2018) 12–17.
- [8] J.J. Spivey, Complete catalytic oxidation of volatile organicst, *Ind. Eng. Chem. Res.* 26 (1987) 2165–2180.
- [9] G. Spezzati, A.D. Benavidez, A.T. DeLaRiv, Y. Su, J.P. Hofmann, S. Asahin, E.J. Olivier, J.H. Neethling, J.T. Millere, A.K. Datye, E.J.M. Hensen, CO oxidation by Pt supported on $\text{CeO}_2(100)$ and $\text{CeO}_2(111)$ facets, *Appl. Catal. B: Environ.* 243 (2019) 36–46.
- [10] Y. Xie, J. Wu, G. Jing, H. Zhang, S. Zeng, X. Tian, X. Zou, J. Wen, H. Su, C. Zhong, P. Cui, Structural origin of high catalytic activity for preferential CO oxidation over CuO/CeO_2 nanocatalysts with different shapes, *Appl. Catal. B: Environ.* 239 (2018) 665–676.
- [11] S. Xie, Y. Liu, J. Deng, X. Zhao, J. Yang, K. Zhang, Z. Han, H. Arandiyan, H. Dai, Effect of transition metal doping on the catalytic performance of $\text{Au-Pd}/3\text{DOM Mn}_2\text{O}_3$ for the oxidation of methane and o-xylene, *Appl. Catal. B: Environ.* 206 (2017) 221–232.
- [12] L. Nie, J. Yu, X. Li, B. Cheng, G. Liu, M. Jaroniec, Enhanced performance of NaOH-Modified Pt/TiO₂ toward room temperature selective oxidation of formaldehyde, *Environ. Sci. Technol.* 47 (2013) 2777–2783.
- [13] R. Peng, S. Li, X. Sun, Q. Ren, L. Chen, M. Fu, J. Wu, D. Ye, Size effect of Pt nanoparticles on the catalytic oxidation of toluene over Pt/CeO₂ catalysts, *Appl. Catal. B: Environ.* 220 (2018) 462–470.
- [14] H. Deng, S. Kang, J. Ma, C. Zhang, H. He, Silver incorporated into cryptomelane-type Manganese oxide boosts the catalytic oxidation of benzene, *Appl. Catal. B: Environ.* 239 (2018) 214–222.
- [15] F. Wang, H. Dai, J. Deng, G. Bai, K. Ji, Y. Liu, Manganese oxides with Rod-, wire-, tube-, and flower-like morphologies: highly effective catalysts for the removal of toluene, *Environ. Sci. Technol.* 46 (2012) 4034–4041.
- [16] W. Si, Y. Wang, Y. Peng, X. Li, K. Li, J. Li, A high-efficiency $\gamma\text{-MnO}_2$ -like catalyst in toluene combustion, *Chem. Commun. (Camb.)* 51 (2015) 14977–14980.
- [17] W. Tang, X. Wu, D. Li, Z. Wang, G. Liu, H. Liu, Y. Chen, Oxalate route for promoting activity of manganese oxide catalysts in total VOCs oxidation: effect of calcination temperature and preparation method, *J. Mater. Chem. A Mater. Energy Sustain.* 2 (2014) 2544–2554.
- [18] J. Chen, X. Chen, W. Xu, Z. Xu, J. Chen, H. Jia, J. Chen, Hydrolysis driving redox reaction to synthesize Mn-Fe binary oxides as highly active catalysts for the removal of toluene, *Chem. Eng. J.* 330 (2017) 281–293.
- [19] Y. Huang, K. Ye, H. Li, W. Fan, F. Zhao, Y. Zhang, H. Ji, A highly durable catalyst based on $\text{Co}_x\text{Mn}_{3-x}\text{O}_4$ nanosheets for low-temperature formaldehyde oxidation, *Nano Res.* 9 (12) (2016) 3881–3892.
- [20] F. Hu, Y. Peng, J. Chen, S. Liu, H. Song, J. Li, Low content of CoO_x supported on nanocrystalline CeO_2 for toluene combustion: the importance of interfaces between active sites and supports, *Appl. Catal. B: Environ.* 240 (2019) 329–336.
- [21] C. Wang, C. Zhang, W. Hua, Y. Guo, G. Lu, S. Gil, A. Giroir-Fendler, Catalytic oxidation of vinyl chloride emissions over Co-Ce composite oxide catalysts, *Chem. Eng. J.* 315 (2017) 392–402.
- [22] Z. Hu, S. Qiu, Y. You, Y. Guo, L. Wang, W. Zhan, G. Lu, Hydrothermal synthesis of NiCeO_x nanosheets and its application to the total oxidation of propane, *Appl. Catal. B: Environ.* 225 (2018) 110–120.
- [23] L. Huang, M. Zheng, D. Yu, M. Yaseen, L. Duan, W. Jiang, L. Shi, In-situ fabrication and catalytic performance of Co-Mn@CuO core-shell nanowires on copper meshes/foams, *Mater. Design.* 147 (2018) 182–190.
- [24] Y. Sun, Z. Yang, P. Tian, Y. Sheng, J. Xu, Y. Han, Oxidative degradation of nitrobenzene by a Fenton-like reaction with Fe-Cu bimetallic catalysts, *Appl. Catal. B: Environ.* 244 (2019) 1–10.
- [25] P. Yang, S. Fan, Z. Chen, G. Bao, S. Zuo, C. Qi, Synthesis of Nb_2O_5 based solid superacid materials for catalytic combustion of chlorinated VOCs, *Appl. Catal. B: Environ.* 239 (2018) 114–124.
- [26] Q. Ren, S. Mo, R. Peng, Z. Feng, M. Zhang, L. Chen, M. Fu, J. Wu, D. Ye, Controllable synthesis of 3D hierarchical Co_3O_4 nanocatalysts with various morphologies for the catalytic oxidation of toluene, *J. Mater. Chem. A Mater. Energy Sustain.* 6 (2018) 498–509.
- [27] G. Li, C. Zhang, Z. Wang, H. Huang, H. Peng, X. Li, Fabrication of mesoporous Co_3O_4 oxides by acid treatment and their catalytic performances for toluene oxidation, *Appl. Catal. A Gen.* 550 (2018) 67–76.
- [28] J. González-Prior, R. López-Fonseca, J.I. Gutiérrez-Ortiz, B. de Rivas, Catalytic removal of chlorinated compounds over ordered mesoporous cobalt oxides synthesised by hard-templating, *Appl. Catal. B: Environ.* 222 (2018) 9–17.
- [29] L. Lin, Bai H, Salt-induced formation of hollow and mesoporous $\text{CoO}_x/\text{SiO}_2$ spheres and their catalytic behavior in toluene oxidation, *RSC Adv.* 6 (2016) 24304–24313.
- [30] X. Wang, Y. Liu, T. Zhang, Y. Luo, Z. Lan, K. Zhang, J. Zuo, L. Jiang, R. Wang,

Geometrical-site-Dependent catalytic activity of ordered mesoporous Co-based spinel for benzene oxidation: in situ DRIFTS study coupled with Raman and XAFS spectroscopy, *ACS Catal.* 7 (2017) 1626–1636.

[31] Y. Luo, K. Wang, J. Zuo, Q. Qian, Y. Xu, X. Liu, H. Xue, Q. Chen, Selective corrosion of LaCoO₃ by NaOH: structural evolution and enhanced activity for benzene oxidation, *Catal. Sci. Technol.* 7 (2017) 496–501.

[32] C. Lahousse, A. Bernier, P. Grange, B. Delmon, P. Papaefthimiou, T. Ioannides, X. Verykios, Evaluation of γ -MnO₂ as a VOC removal catalyst: comparison with a noble metal catalyst, *J. Catal.* 178 (1998) 214–225.

[33] H. He, X. Lin, S. Li, Z. Wu, J. Gao, J. Wu, W. Wen, D. Ye, M. Fu, The key surface species and oxygen vacancies in MnO_x(0.4)-CeO₂ toward repeated soot oxidation, *Appl. Catal. B: Environ.* 223 (2018) 134–142.

[34] Q. Xiong, J. Tu, S. Shi, X. Liu, X. Wang, C. Gu, Ascorbic acid-assisted synthesis of cobalt ferrite (CoFe₂O₄) hierarchical flower-like microspheres with enhanced lithium storage properties, *J. Power Sources* 256 (2014) 153–159.

[35] J. Xu, D. Su, W. Bao, Y. Zhao, X. Xie, G. Wang, Rose flower-like NiCo₂O₄ with hierarchically porous structures for highly reversible lithium storage, *J. Alloys Compd.* 684 (2016) 691–698.

[36] Z. Wang, G. Shen, J. Li, H. Liu, Q. Wang, Y. Chen, Catalytic removal of benzene over CeO₂-MnO_x composite oxides prepared by hydrothermal method, *Appl. Catal. B: Environ.* 138–139 (2013) 253–259.

[37] X. Wang, Q. Kang, D. Li, Catalytic combustion of chlorobenzene over MnO_x-CeO₂ mixed oxide catalysts, *Appl. Catal. B: Environ.* 86 (2009) 166–175.

[38] J. Chen, X. Chen, X. Chen, W. Xua, Z. Xua, H. Jia, Jing Chen, Homogeneous introduction of CeO₂ into MnO_x-based catalyst for oxidation of aromatic VOCs, *Appl. Catal. B: Environ.* 224 (2018) 825–835.

[39] Y. Han, L. Chen, K. Ramesh, E. Widjaja, S. Chilukoti, I.K. Surjami, J. Chen, Kinetic and spectroscopic study of methane combustion over α -Mn₂O₃ nanocrystal catalysts, *J. Catal.* 253 (2008) 261–268.

[40] D. Delimaris, T. Ioannides, VOC oxidation over MnO_x-CeO₂ catalysts prepared by a combustion method, *Appl. Catal. B: Environ.* 84 (2008) 303–312.

[41] Y. Li, Y. Li, P. Wang, W. Hu, S. Zhang, Q. Shi, S. Zhan, Low-temperature selective catalytic reduction of NO_x with NH₃ over MnFeO_x nanorods, *Chem. Eng. J.* 330 (2017) 213–222.

[42] J. Xu, Y. Deng, Y. Luo, W. Mao, X. Yang, Y. Han, Operando Raman spectroscopy and kinetic study of low-temperature CO oxidation on an a-Mn₂O₃ nanocatalyst, *J. Catal.* 300 (2013) 225–234.

[43] S. Zhang, Y. Guo, X. Li, Z. Li, Effects of cerium doping position on physicochemical properties and catalytic performance in methanol total oxidation, *J. Rare Earths* 36 (2018) 811–818.

[44] P. Venkataswamy, K.N. Rao, D. Jampaiah, B.M. Reddy, Nanostructured manganese doped ceria solid solutions for CO oxidation at lower temperatures, *Appl. Catal. B: Environ.* 162 (2015) 122–132.

[45] Y. Liao, M. Fu, L. Chen, J. Wu, B. Huang, D. Ye, Catalytic oxidation of toluene over nanorod-structured Mn-Ce mixed oxides, *Catal. Today* 216 (2013) 220–228.

[46] Z. Sihai, F. Puleo, J.M. Garcia-Vargas, L. Retailleau, C. Descomme, L.F. Liotta, J.L. Valverde, S. Gil, A. Giroir-Fendler, Manganese oxide-based catalysts for toluene oxidation, *Appl. Catal. B: Environ.* 209 (2017) 689–700.

[47] M. Piumetti, D. Fino, N. Russo, Mesoporous manganese oxides prepared by solution combustion synthesis as catalysts for the total oxidation of VOCs, *Appl. Catal. B: Environ.* 163 (2015) 277–287.

[48] Z. Ye, J.-M. Giraudon, N. Nuns, P. Simon, N. De Geyter, R. Morent, J.-F. Lamonier, Influence of the preparation method on the activity of copper-manganese oxides for toluene total oxidation, *Appl. Catal. B: Environ.* 223 (2018) 154–166.

[49] P. Li, Y. Xin, Q. Li, Z. Wang, Z. Zhang, L. Zheng, Ce-Ti amorphous oxides for selective catalytic reduction of NO with NH₃: confirmation of Ce-O-Ti active sites, *Environ. Sci. Technol.* 46 (2012) 9600–9605.

[50] X. Lin, S. Li, H. He, Z. Wu, J. Wu, L. Chen, D. Ye, M. Fu, Evolution of oxygen vacancies in MnO_x-CeO₂ mixed oxides for soot oxidation, *Appl. Catal. B: Environ.* 223 (2018) 91–102.

[51] L. Ma, C.Y. Seo, M. Nahata, X. Chen, J. Li, J. Schwank, Shape dependence and sulfate promotion of CeO₂ for selective catalytic reduction of NO_x with NH₃, *Appl. Catal. B: Environ.* 232 (2018) 246–259.

[52] D. Jampaiah, K.M. Tur, P. Venkataswamy, S.J. Ippolito, Y.M. Sabri, J. Tardio, S.K. Bhargava, B.M. Reddy, Catalytic oxidation and adsorption of elemental mercury over nanostructured CeO₂-MnO_x catalyst, *RSC Adv.* 5 (2015) 30331–30341.

[53] Y. Li, Q. Sun, M. Kong, W. Shi, J. Huang, J. Tang, X. Zha, Coupling oxygen ion conduction to photocatalysis in mesoporous nanorod-like ceria significantly improves photocatalytic efficiency, *J. Phys. Chem. C* 115 (2011) 14050–14057.

[54] Z. Zhang, L. Chen, Z. Li, P. Li, F. Yuan, X. Niu, Y. Zhu, Activity and SO₂ resistance of amorphous Ce_aTiO_x catalysts for the selective catalytic reduction of NO with NH₃: in situ DRIFT studies, *Catal. Sci. Technol.* 6 (2016) 7151–7162.

[55] X. Leng, Z. Zhang, Y. Li, T. Zhang, S. Ma, F. Yuan, X. Niu, Y. Zhu, Excellent low temperature NH₃-SCR activity over Mn_aCe_{0.3}TiO_x ($a = 0.1$ – 0.3) oxides: influence of Mn addition, *Fuel Process. Technol.* 181 (2018) 33–43.

[56] W.B. Li, Z.X. Liu, R.F. Liu, J.L. Chenab, B.Q. Xu, Rod-like CuMnO_x transformed from mixed oxide particles by alkaline hydrothermal treatment as a novel catalyst for catalytic combustion of toluene, *Phys. Chem. Chem. Phys.* 18 (2016) 22794–22798.

[57] J. Li, E. Yu, S. Cai, X. Chen, J. Chen, H. Jia, Y. Xu, Noble metal free, CeO₂/LaMnO₃ hybrid achieving efficient photo-thermal catalytic decomposition of volatile organic compounds under IR light, *Appl. Catal. B: Environ.* 240 (2019) 141–152.

[58] C. Wang, S. Lin, C. Chen, H. Weng, Performance of the supported copper oxide catalysts for the catalytic incineration of aromatic hydrocarbons, *Chemosphere* 64 (2006) 503–509.

[59] X. Wang, W. Zhao, X. Wu, T. Zhang, Y. Liu, K. Zhang, Y. Xiao, L. Jiang, Total oxidation of benzene over ACo204 (A = Cu, Ni and Mn) catalysts: in situ DRIFTS account for understanding the reaction mechanism, *Appl. Surf. Sci.* 426 (2017) 1198–1205.

[60] S. Besselmann, E. Löffler, M. Muhler, On the role of monomeric vanadyl species in toluene adsorption and oxidation on V₂O₅/TiO₂ catalysts: a Raman and in situ DRIFTS study, *J. Mater. Chem. A Mater. Energy Sustain.* 162 (2000) 401–411.

[61] S. Zhao, F. Hu, J. Li, Hierarchical core–Shell Al₂O₃@Pd-CoAlO microspheres for LowTemperature toluene combustion, *ACS Catal.* 6 (2016) 3433–3441.

[62] F. Hayatama, T. Ohno, T. Maruoka, H. Miyata, Reactivities of m-xylene, phenol and benzene on vanadium oxides ayered on TiO₂ and ZrO₂, *Catal. Lett.* 45 (1991) 265–269.

[63] K. Li, J. Chen, B. Bai, S. Zhao, F. Hu, J. Li, Bridging the reaction route of toluene total oxidation and the structure of ordered mesoporous Co₃O₄: the roles of surface sodium and adsorbed oxyge, *Catal. Today* 297 (2017) 173–181.

[64] C. Chang, Z. Huang, J. Li, The promotional role of water in heterogeneous catalysis: mechanism insights from computational modeling, *Wiley interdisciplinary reviews, Comput. Mol. Sci.* 6 (2016) 679–693.

[65] A. Bongiorno, U. Landman, Water-enhanced catalysis of CO oxidation on free and supported gold nanoclusters, *Phys. Rev. Lett.* 95 (2005) 9–13.